

Kinematic Data-Based Action Segmentation for Surgical Applications

Adam Goldbraikh, Omer Shubi, Or Rubin, Carla M Pugh, and Shlomi Laufer

Abstract—Action segmentation is a challenging task in high-level process analysis, typically performed on video or kinematic data obtained from various sensors. In the context of surgical procedures, action segmentation is critical for workflow analysis algorithms. This work presents two contributions related to action segmentation on kinematic data. Firstly, we introduce two multi-stage architectures, MS-TCN-BiLSTM and MS-TCN-BiGRU, specifically designed for kinematic data. The architectures consist of a prediction generator with intra-stage regularization and Bidirectional LSTM or GRU-based refinement stages. Secondly, we propose two new data augmentation techniques, World Frame Rotation and Horizontal-Flip, which utilize the strong geometric structure of kinematic data to improve algorithm performance and robustness. We evaluate our models on three datasets of surgical suturing tasks: the Variable Tissue Simulation (VTS) Dataset and the newly introduced Bowel Repair Simulation (BRS) Dataset, both of which are open surgery simulation datasets collected by us, as well as the JHU-ISI Gesture and Skill Assessment Working Set (JIGSAWS), a well-known benchmark in robotic surgery. Our methods achieve state-of-the-art performance on all benchmark datasets and establish a strong baseline for the BRS dataset.

Index Terms—Action segmentation, Motion sensor, Surgical workflow analysis, and Surgical data science

1 INTRODUCTION

1.1 Background

The problem of action segmentation is one of the most challenging in high-level process analysis. Essentially, action segmentation consists of segmenting a temporally untrimmed sequence by labeling each segmented part. Typically, action segmentation is performed on video data [1], [2], [3], [4], [5], [6], [7], on kinematic data acquired from various sensors [8], [9], [10], [11] or even multi-modal approaches that combine different types of data [12], [13], [14]. A significant role is played by automatically segmenting long untrimmed data sequences for the purposes of understanding human-to-human or human-to-robot relations interaction. There is a significant benefit to understanding what actions are being performed, when they began, how far they have progressed, what kind of transformations are being brought to the environment as a result of these actions, and what people will do next. There is a wide range of potential applications of these segmentation methods that can have a significant impact on the day-to-day lives of humans, such as video security and surveillance systems, human-robot interaction, assistive systems, and automatic video summarization systems.

In the context of surgical procedures, action segmentation is typically used as part of workflow analysis algorithms. The workflow can be divided into increasingly specific levels of granularity, beginning with dividing the procedure into phases, then dividing phases into steps, then steps into maneuvers, and finally dividing maneuvers into elementary actions called gestures.

Historically, as the camera plays a vital role in minimally invasive surgery (MIS) such as laparoscopic and robotic-assisted minimally invasive surgery (RAMIS), it was natural to make use of an algorithm to process this information. Besides the video data, RAMIS can also capture kinematic data in real-time. Hence, kinematic data-based algorithms for workflow analysis were also developed. A variety of datasets were collected by RAMIS systems, including video and kinematics of the robot as well as manual annotation of activities and skill assessment [12], [15]. Nowadays, the benefits of using deep learning algorithms in open surgery are clear, and there is a growing interest in the development of open surgery capturing methods [16], [17], [18]. A number of datasets of open surgery procedures have been presented, as well as algorithms for equivalent open surgery tasks [8], [17], [19], [20].

In RAMIS, the JHU-ISI Gesture and Skill Assessment Working Set (JIGSAWS dataset) includes kinematic data captured using the da Vinci robot [15]. There have been several studies that have applied this kinematic data to gesture recognition, using Convolutional Neural Networks (CNNs) [21] and Recurrent Neural Networks (RNNs) [10], [11] as well as Temporal Convolutional Networks (TCNs) [22]. Additionally, multiple studies have used video or multimodal approaches on this dataset [1], [7], [13], [23].

In [8] we analyzed open surgery simulator data collected with six degrees of freedom (6 DOF) motion sensors placed on surgeons' hands. Based solely on kinematic data, ges-

- A. Goldbraikh is with the Applied Mathematics Department at the Technion – Israel Institute of Technology, Haifa 3200003, Israel (e-mail: goldb.adam@gmail.com).
- CM Pugh is with Stanford University, School of Medicine Stanford, CA, USA (e-mail: cpugh@stanford.edu).
- O. Shubi (e-mail: shubi@campus.technion.ac.il), O. Rubin (e-mail: orrubin@campus.technion.ac.il), and S. Laufer (e-mail: laufer@technion.ac.il) are with the Faculty of Data and Decision Sciences at the Technion – Israel Institute of Technology, Haifa 3200003, Israel.
- The work was supported by the National Institutes of Health R01DK123445.

tures and tools were recognized. This study [8] was the first to use kinematic data to recognize gestures in open surgery, to our knowledge. In [8] strong baselines were established for *Bidirectional Gated Recurrent Unit Network* (BiGRU), *Bidirectional Long Short-Term Memory Network* (BiLSTM), and *Multi-Stage Temporal Convolutional Network* (MS-TCN++) on both gesture recognition and tool recognition tasks using sensor motion data, where the sensor-adapted MS-TCN++ outperforms other networks in the gesture recognition task.

In data augmentation, existing data is utilized to generate new data instances to artificially increase their quantity, thus improving the algorithm’s generalization. Traditionally, amplification is achieved by adding minor changes to data. Recently, machine and deep learning generative models have been used to generate new data based on a given dataset, and data augmentation has gained popularity as part of self-supervised learning problems [24], [25], [26], [27].

Most of the data augmentation research is dedicated to the computer vision field. Data augmentations in computer vision contain classical image transformation such as cropping, zooming, horizontal flip, rotation, and histogram-based methods, as well as advanced methods like Generative Adversarial Networks and Style Transfer [28].

Augmenting time series data is considered a challenging task. In recent years, a few studies presented data augmentation methods that can be divided into four general families, including transformation-based methods, decomposition methods, pattern mixing approaches, and generative models [29]. In models that rely on electromagnetic sensor kinematic data, data augmentation is rare, despite the fact that they are time series data. In contrast to standard time series data like stock prices or patient health monitoring, such as an electrocardiogram (ECG), here there is a geometrical meaning to the values. Namely, there is 3D spatial information for each sensor, e.g., we expect a high correlation between velocities and positions of the sensors that are placed on the same hand. The geometric interpretation of the information from the sensors makes it worthwhile to search for augmentations on the basis of geometric relations. For the first time in [30], [31], geometrical factors were taken into account in the development of the augmentation of kinematic data.

1.2 Our Contribution

This work aims to achieve two goals related to action segmentation tasks on kinematic data: the creation of new architectures and the development of data augmentations that are geometrically oriented.

Firstly, we introduce two multi-stage architectures, MS-TCN-BiLSTM and MS-TCN-BiGRU, that have been specifically designed for kinematic data and demonstrate state-of-the-art results on benchmark datasets. The main components of our new architectures are as follows:

- A prediction generator with intra-stage regularization.
- BiRNN- based refinement stages.

Intra-stage regularization is a technique that involves adding prediction heads after the internal dual dilated layers of the prediction generator. This improves the frame-wise performance of the network. In the BiRNN-based

refinement stages, downsampling is applied to the input before it is fed into the BiRNN unit and upsampling is applied to the output. As a result, the network’s segmental performance is significantly improved and over-segmentation errors are greatly reduced.

To achieve the second goal, we propose two new data augmentation techniques for kinematic data, which take advantage of the data’s strong geometric structure to improve the performance and robustness of algorithms. Specifically, we propose:

- World Frame Rotation augmentation.
- Horizontal-Flip augmentation.

The World Frame Rotation augmentation is inspired by image rotation. Based on three random Euler angles in a predetermined continuous range, we calculate an augmentation rotation matrix that multiplies the sensors’ location coordinates and its original rotation matrix, which determines its real orientation. Since the same rotation matrix rotates all samples in the time series from all sensors, this is equivalent to rotating the world coordinate system.

Our Horizontal Flip augmentation is inspired by a common horizontal flip of images, adapted to kinematic sensors. Here we calculate a plane that optimally separates the surgeon’s right and left hand over time, reflects the data points across this plane, and exchanges each sensor’s id with the corresponding sensor from the other hand.

2 RELATED WORK

2.1 Action Segmentation

Early methods of segmentation of temporal action relied on hand-crafted features that were used to classify actions in a temporal direction using sliding windows jointly with non-maximum suppression along frames that indicated the temporal direction of the action [32], [33]. Due to the fact that the model needs to be evaluated at different window scales, such approaches are computationally expensive. In [34] the authors use a Bayesian non-parametric model of discrete sequences to classify and segment video sequences by representing videos as sequences of visual words. Although previous approaches were considered successful, they had limited success in capturing long temporal context. In an attempt to alleviate this problem, many proposals used high-level temporal models over frame-wise classifiers. In [35], [36] combined a set of hidden Markov models (HMM), which model the actions, with context-free grammar or with a Gaussian mixture model (GMM). RNNs are another approach to capturing these long-term relationships [37], [38]. The most recent approaches are based on transformer models as in [2] and temporal convolutional neural networks [22]. MS-TCN++ [1] is a *multi-stage* (MS) *temporal convolutional neural network* (TCN) originally intended for action segmentation, using video data as the raw input. The MS-TCN++ presents a *multi-stage framework*. It consists of a prediction generator that produces the initial predictions of the network, which are fed through several refinement stages, such that each stage outputs a prediction of the network. The loss is calculated with respect to the outputs of all stages. The processed input to this network consists of a feature vector for each video frame. This is usually extracted from a 3D CNN, such as I3D [39].

2.2 Kinematic Data and Networks

A variety of methods have been suggested for action segmentation using surgical kinematic data. Earlier approaches were based on probabilistic graphical models [40], [41], [42]. This family of models relies mainly on local transitions, thus losing relationships between long-range temporal events. An approach using surgical kinematic data was proposed in [43], in which the continuous kinematic data is first discretized, both in the time domain and in the sensor values, into predefined bins and segments. After an additional transformation, cosine similarity is used to classify the gesture segments. Another approach that uses surgical kinematic signals as input was proposed in [11]. Their method utilizes a multi-task RNN, predicting surgical gestures and surgical task progress in parallel. Performing both maneuver and gesture recognition, [9] assesses a variety of RNNs, specifically simple RNNs, LSTMs, GRUs, and mixed-history RNNs. Most related to our work are [3], [22] which introduce TCNs, which aim to capture both long-range dependencies and detailed relations between timestamps while doing so faster than RNNs. In [8] MS-TCN++ has been adapted to 6 DOF kinematic data. In [44] inertial measurement unit (IMU) sensors in smartwatches provided three-dimensional orientation and linear and angular motion. After extracting features from the raw data, a BiLSTM was used for classification. Similarly, [45] used multiple on-body IMU sensors as input and a hybrid CNN-LSTM model. Sensor-based applications are not limited only to IMU sensors and can include electromagnetic motion sensors and more.

2.3 Temporal Data Augmentations

There are several techniques for general time-series data augmentation, ranging from relatively simple transformations in the time and frequency domains to more advanced decompositional, statistical, and deep-learning-based methods (see [46] for a review). In [47] numerous augmentations for IMU sensors on construction equipment are given. These include temporal augmentations such as adding jitters, scaling, rotation of individual sensors, and time warping. For surgical gesture recognition, and to improve generalization between dry-lab data and clinical-like data, [30] proposes rotating individual sensors in individual axes. They show that deterministic rotations of the data points impact the classification results. Further, [31] suggests augmenting datasets by exchanging between right- and left-hand surgeon’s data, to account for the imbalance in the number of left-handed surgeons in existing datasets.

3 DATASETS

We evaluated the proposed models on three different datasets of surgical suturing task: the Variable Tissue Simulation (VTS) Dataset [8], [19], [48], [49], the Bowel Repair Simulation (BRS) Dataset [17], [20], and the JHU-ISI Gesture and Skill Assessment Working Set (JIGSAWS) [15] (see Fig.1). VTS and BRS are open surgery simulation datasets, collected by us, while JIGSAWS is a well-known benchmark that contains three elementary surgical training tasks: suturing, knot tying, and needle passing, performed

on the da Vinci Surgical System simulator. The BRS dataset is presented here for the first time in the context of the action segmentation by kinematic data. Firstly, we describe the unique parts of the VTS (Sec. 3.1) and BRS (Sec. 3.2) datasets, then in Sec. 3.3 we describe the shared technical components. Finally, in Sec. 3.4, we describe the JIGSAWS dataset.

3.1 Variable Tissue Simulation (VTS) Dataset

A simulated suturing task was performed with the variable tissue simulator, for the purpose of enhancing decision-making through variation in materials and difficulty [19], [50]. Two opposing sections of material were to be stitched with three interrupted instrument-tied sutures. There were two different types of materials included in the experiment: tissue paper resembling friable tissue, and rubber balloons simulating arteries. With each material, the task was repeated twice. In this study, eleven medical students, thirteen attending surgeons, and one resident participated in the study, completing a total of 100 procedures, each lasting approximately 2-6 minutes. In the VTS dataset, six gestures were identified as part of the suturing task: background gesture, passing the needle through the material, pulling the suture, performing an instrumental tie, laying the knot, and cutting the suture.

3.2 Bowel Repair Simulation (BRS) Dataset

The data was collected using a simulator that represented an operating room trauma patient with an abdominal gunshot wound. In the simulator, porcine intestines and artificial blood were arranged on a tray. At the border of the antimesenteric system, two full-thickness injuries were applied close together. One hole was approximately $1cm^2$ with jagged edges, while the other was smaller, approximately $0.25cm^2$. The repair was completed using all necessary open surgical instruments, excluding electrocautery and staplers. During the procedure, each participant received an assistant at the level of a first-year medical student. On average, it took most participants approximately ten minutes to complete the exercise. In the entire dataset, there were 255 porcine enterotomy repair procedures conducted by different surgeons with various levels of skills. We defined five different surgical maneuvers: suture throws, knot ties performed by an instrument, knot ties performed by hand, thread cuts, and the background maneuver. Among the participants, we identified 52 that performed a single-layer repair on the large hole. We annotated only the suturing part of the procedure on these participants. Hence, there are 52 sequences in this dataset. In Fig.2 a detailed dataset analysis is presented, including the frequency and duration of each maneuver. Out of 52 participants, 45 were right-handed, three were left-handed, three were ambidextrous, and one had unknown handedness.

3.3 VTS and BRS Data Acquisition and Preprocessing

Motion data was captured using electromagnetic motion sensors (Ascension, trackSTAR Model 180). Three sensors were taped to the index, thumb, and wrist of each participant’s hands under the surgical gloves. Video data was captured using two cameras, one closeup camera focusing on

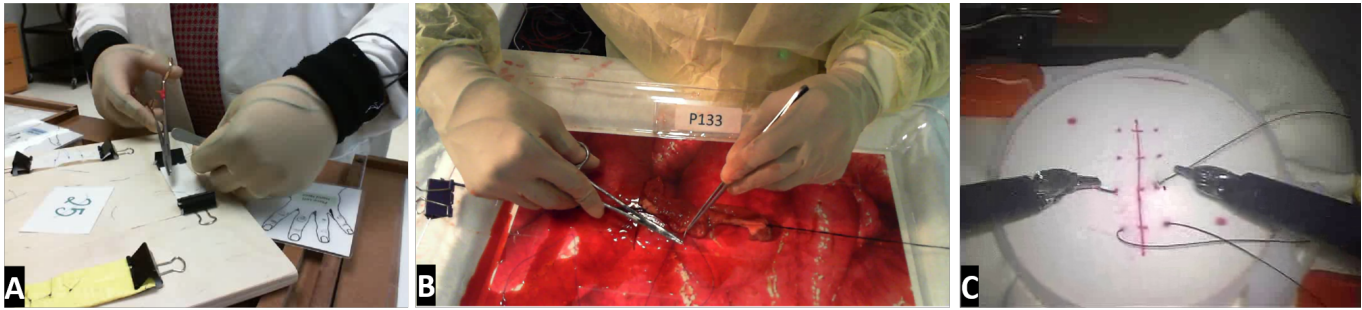


Fig. 1. The three datasets we used to evaluate our algorithms and augmentations. A- Variable Tissue Simulation Dataset, B- Bowel Repair Simulation Dataset and, C- JHU-ISI Gesture and Skill Assessment Working Dataset

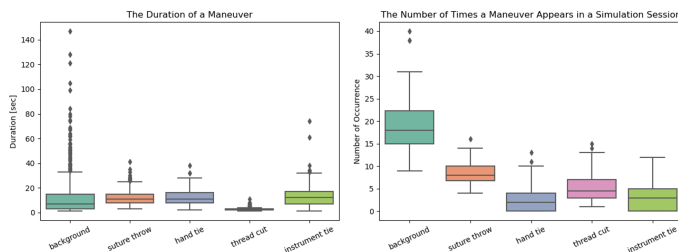


Fig. 2. An illustration of the distributions of maneuvers in the BRS dataset in a box-plot with whiskers, drawn within the 1.5 IQR value. The left figure represents the distribution of the duration of a single instance of maneuver, and the right figure represents the distribution of the number of instances during a procedure of each type of maneuver.

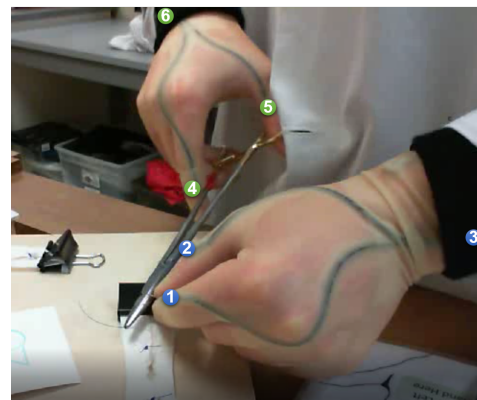


Fig. 3. Participants' hands with sensors. A picture from the VTS dataset, but in the BRS dataset the sensors are located in the same locations.

the simulation area and one overview camera that included the surrounding area. The sensors and both cameras were captured and synchronized using MotionMonitor software (Innovative Sports Training, Inc.). The labeling process was conducted using the Behavioral Observation Research Interactive Software (BORIS) [51] and relied on video data. Each activity, including gestures and maneuvers, was defined by its respective start and end times. The raw data contains for each electromagnetic sensor three coordinates indicating the location of the sensor in space, and three Euler angles indicating the sensor's orientation for a total of 36 kinematic variables for each timestamp. The original measurement rate was $179.695Hz$ in VTS and $100Hz$ in BRS datasets. The data from both datasets have been downsampled to $30Hz$ after filtering with an FIR low pass filter. The filter was designed with the Parks-MacClellan algorithm [52]. The pass-band cutoff frequency was $10Hz$ with a ripple of $3.91dB$, and the stopband cutoff frequency was $15Hz$ with a ripple of $-33.511dB$.

3.4 JHU-ISI Gesture and Skill Assessment Working Set (JIGSAWS)

In this study, eight surgeons with different skill levels performed five repetitions of three elementary surgical tasks on a benchtop model using the da Vinci Surgical System: suturing, knotting, and needle passing, which are standard components of surgical skills training. The dataset contains stereo video data, kinematic data, and manual annotations of gestures and skills scoring. Consistent with previous research, our work focuses on the suturing task, which

involves ten distinct gestures including G1-Reaching for the needle with the right hand, G2-Positioning needle, G3-Pushing needle through tissue, G4-Transferring needle from left to right, G5-Moving to center with a needle in grip, G6-Pulling suture with a left hand, G8-Orienting needle, G9-Using right hand to help tighten suture, G10-Loosening more suture, and G11-Dropping suture at end and moving to end points. The Kinematic data includes data from the two patient side manipulators (PSMs) and master tool manipulators (MTMs). Each PSM's data includes the cartesian positions, a rotation matrix, linear velocities, angular velocities, and a gripper angle of the manipulator. Here, for each manipulator, we used only three position variables, calculated three Euler angles based on the rotation matrix data, and the gripper angle, in total 14 kinematic variables. We used the corrected version of the labels, as it was used in [11]. As the kinematic data in the JIGSAWS dataset is already provided at $30Hz$, we did not filter this data.

4 ACTION SEGMENTATION

Using kinematic data as inputs, we introduce a new, multi-stage network that consists of a temporal convolutional prediction generator in conjunction with a *recurrent neural network* (RNN) based refinement stage for the action segmentation task. We refer to RNN as the generic name for several well-known algorithms including *Bidirectional Long short-term memory (BiLSTM) networks* and *Bidirectional*

Gated recurrent units (BiGRUs). In action segmentation, given the sequence of vectors including the kinematic data for each timestamp $x_{1:T} = (x_1, \dots, x_T)$, the algorithm’s goal is to predict one label out of a pre-defined set of classes for each data point. Let $y_i \in \{1, \dots, C\} : i \in [1, T]$ be the ground truth label for the i^{th} timestamp, and $Y = (y_1, \dots, y_T) \in \mathbb{R}^T$ be the ground truth sequence, where C is the number of classes and T is the sequence length. The output of the algorithm is a sequence of probabilities vectors $\hat{Y} = (\hat{y}_1, \dots, \hat{y}_T) \in \mathbb{R}^{C \times T}$.

4.1 MS-TCN-BiRNN

In the multi-stage framework, there are several models stacked in a sequential manner so that each model’s output is used as input for the subsequent model in the chain that refines it. Several tasks, including action segmentation in MS-TCN++, have been found to benefit from the use of this method as a performance enhancer. In this chain, the first model serves as a prediction generator, PG , and the rest as refinement stages, where $Ref_j : j \in \mathbb{N}_+$ is the j^{th} refinement stage, as depicted in Fig.4. Formally, the multi-stage framework is defined as follows:

$$\hat{Y}_0 = PG(x_{1:T}) \quad (1)$$

$$\hat{Y}_j = Ref_j(\hat{Y}_{j-1}) \quad (2)$$

Where \hat{Y}_0 is the output of the prediction generator and $\hat{Y}_j : j \in \mathbb{N}_+$ is the output of the j^{th} refinement stage. We would like to point out that in our framework, the input to the refinement stages is just the frame-wise probabilities, without additional information or features from the deeper layers of the model.

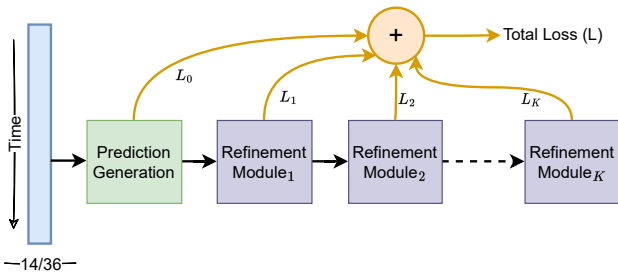


Fig. 4. General structure of the multi-stage network

4.1.1 Prediction Generation Module

We based our prediction generator on the prediction generator of MS-TCN++ with additional prediction heads added inside the stage. By having these heads, the system can be forced to classify actions based on partial information, with a greater focus placed on the classification data point region, rather than relying solely on the full context obtained in the output of the stage. Hence, we called this method intra-stage regularization (ISR). This method was found to be beneficial to the frame-wise performance of the system.

We will first discuss the conventional prediction generator as stated in [1], and then we will offer our ISR extension.

The standard prediction generator consists only of temporal convolutional layers, which allow handling varying input lengths. To match the input dimensions

of the stage with the number of feature maps, the input of the prediction generation unit passes through a 1×1 convolutional layer. Then, these features are fed into several *Dual Dilated Residual Layers* (DDLRLs), which serve as the prediction generator’s core units. In the standard prediction generator in MS-TCN++, as a final step, the output of the last DDRL is passed through a prediction head that includes a 1×1 convolution to adjust the number of channels to the number of classes. Let’s consider the ℓ^{th} DDRL where $\ell \in \{1, 2, 3 \dots L\}$ and L is the total number of layers. First, the input of the DDRL is entered into two dilated temporal convolution layers (DTCLs) in parallel, with a kernel size of 3, one with a dilation factor of $\delta^1(\ell) = 2^{\ell-1}$ and the other with a dilation factor of $\delta^2(\ell) = 2^{L-\ell}$. The dilation factor determines the distance between kernel elements, such that a dilation of 1 means that the kernel is dense. Then by concatenating the feature in the channel dimension, the outputs of the two dilated convolutional layers are fused and inserted into a 1D convolutional layer to reduce the number of channels back into the constant number of feature maps. The output passes through a ReLU activation and an additional 1D convolutional layer before the residual connection (see Fig.5). formally, the prediction DDRL can be described as follows:

$$\hat{H}_{\delta^1(\ell)} = W_{\delta^1} * H_{\ell-1} + b_{\delta^1} \quad (3)$$

$$\hat{H}_{\delta^2(\ell)} = W_{\delta^2} * H_{\ell-1} + b_{\delta^2} \quad (4)$$

$$\hat{H}_{\ell} = ReLU([\hat{H}_{\delta^1(\ell)}, \hat{H}_{\delta^2(\ell)}]) \quad (5)$$

$$H_{\ell} = H_{\ell-1} + W * \hat{H}_{\ell} + b \quad (6)$$

Where H_{ℓ} is the output of layer ℓ , $[\cdot, \cdot]$ denotes concatenation operator and $*$ is the convolution operator, $W_{\delta^1}, W_{\delta^2} \in \mathbb{R}^{3 \times D \times D}$ are the weights of temporal dilated convolutions such that δ_1, δ_2 are their dilation factors, D is the number of feature maps, and 3 is the kernel size. The weights of the 1×1 convolution are denoted by $W \in \mathbb{R}^{1 \times 2D \times D}$, and $b, b_{\delta^1}, b_{\delta^2} \in \mathbb{R}^D$ are the bias vectors.

Prediction generator with intra-stage regularization (ISR): As described before, the input and the output of each DDRL have the same dimensions. Thus, each such feature map could, in principle, have been passed to an identical prediction head. In practice, only the output of the final layer is passed to the prediction head. We refer to this prediction head as the stage’s prediction head and to its output as the stage’s output. Note that the stage’s output is then fed to the refinement.

In addition, each feature map from a pre-determined set of layers is passed through a prediction head (see Fig.5), and contributes equally to the loss. Let $\hat{H}_{ISR} = \{4, 7, 10\}$ to be a *possible ISR heads indexes set* and $H_{ISR} = \{i \in \hat{H}_{ISR} \mid i < L\}$ to be an *ISR heads indexes set*, namely a set of DDRLs indexes, such that if $i \in H_{ISR}$, then after the i^{th} DDRL in the prediction generator we added a prediction head. Note the stage output head follows layer number L in any case.

The formulation of ISR prediction heads and the stage output head are identical. The prediction heads consist of a 1×1 convolution over the output features of its DDRL, followed by a softmax activation, formally

$$O_{t,\ell} = Softmax(W h_{\ell,t} + b) \quad (7)$$

Where $h_{\ell,t}$ is the output of the ℓ^{th} DDRL at time t , $W \in \mathbb{R}^{1 \times C \times D}$ has the weights of 1×1 convolution and $b \in \mathbb{R}^C$ is the bias. $O_{t,\ell}$ represents the class probabilities of the prediction head that follows the ℓ^{th} DDRL at time t , such that $\ell \in H_{ISR} \cup \{L\}$. In the case that $\ell = L$ it is satisfied that $O_{t,\ell} = \hat{y}_t$, where \hat{y}_t contains the stage's output probabilities at time t .

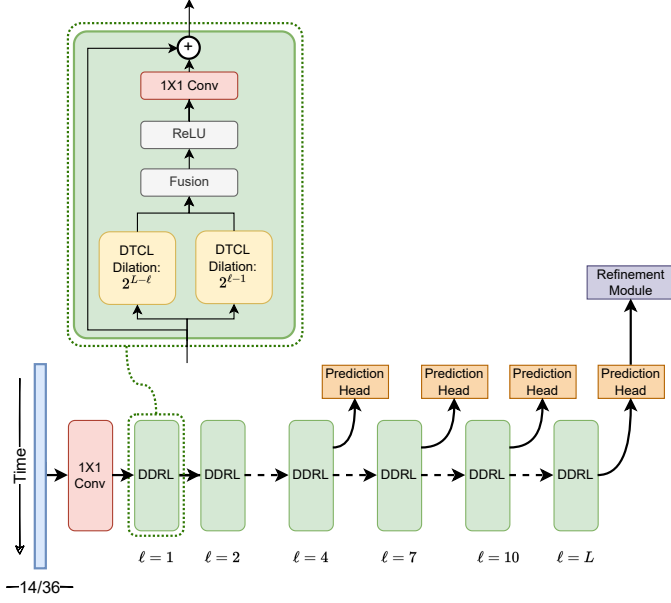


Fig. 5. Prediction generator with intra-unit regularization with a close-up view of a DDRL

4.1.2 Refinement Stages

For the refinement stage, we evaluate RNN-based architectures, BiGRU, and BiLSTM. Our RNN unit is followed by a linear layer for prediction probabilities generation. During training, prior to entering the prediction head, we apply a dropout. In our previous study, we found that the optimal frequency for action segmentation of RNN-based networks for kinematic data is significantly distinct from the optimal input frequency of TCN-based networks [8]. This fact inspired us to feed the refinement stage with a different frequency than our TCN-based prediction generator. Hence, the RNN units input is downsampled by factor k . Since our model is evaluated in the full input's resolution, the output is upsampled back into the original frequency. Downsampling by a factor of k means that every k^{th} element in the sequence is selected; we will mark this operator by $\downarrow k(\cdot)$, namely let $X = (x_1, x_2, \dots, x_N)$ be a sequence of samples $\downarrow k(X) = (x_1, x_{k+1}, \dots, x_{N-(N-1) \bmod k})$, in total $N' = \lfloor (N-1)/k \rfloor + 1$ elements. Our upsampling operator $\uparrow k(\cdot)$ takes every sample in a sequence and replaces it with k copies of this sample, such that let $X = (x_1, x_2, \dots, x_{N'})$ be sequence of samples $\uparrow k(X) = (x_{1,1}, \dots, x_{1,k}, \dots, x_{N',1}, \dots, x_{N',k})$. To define formally the refinement stage we will use $RNN(\cdot)$ to represent any bidirectional function belonging to the RNN family, such as $BiLSTM(\cdot)$ or $BiGRU(\cdot)$. Let $\hat{Y}_j = (\hat{y}_{j,1}, \dots, \hat{y}_{j,T})$ be a probabilities vector obtained from stage number $j \in \mathbb{N}$

which serves as an input to the current refinement stage, and let $k \in \mathbb{N}_+$ be a sampling factor.

$$\bar{Y}_j = \downarrow k(\hat{Y}_j) \quad (8)$$

$$h_i = RNN(\bar{y}_{j,i}) : i \in \{1, \dots, \lfloor (T-1)/k \rfloor + 1\} \quad (9)$$

$$\bar{y}_{j+1,i} = Softmax(Ah_i^\top + b) \quad (10)$$

$$\hat{Y}_{j+1} = \uparrow k(\bar{Y}_{j+1}) \quad (11)$$

Where $h_i \in \mathbb{R}^{1 \times 2Q}$ is the concatenation of forward and reverse hidden states of the last layer in the RNN corresponding to time t , and the hidden size of each RNN is Q . The weights matrix is $A \in \mathbb{R}^{C \times 2Q}$, and $b \in \mathbb{R}^C$ is a bias vector.

4.1.2.1 Basic RNN Units: Let us now formally define $BiLSTM(\cdot)$ and $BiGRU(\cdot)$, which are practical realizations of $RNN(\cdot)$ in equation 9. First, let's define LSTM and GRU units. One of the most widely adopted RNN architectures is the long short-term memory (LSTM), which addresses the vanishing gradient problem [53]. The LSTM unit can be formalized as follows:

$$i_t = \sigma(W_{ii}x_t + W_{hi}h_{t-1} + b_i) \quad (12)$$

$$f_t = \sigma(W_{if}x_t + W_{hf}h_{t-1} + b_f) \quad (13)$$

$$g_t = \tanh(W_{ig}x_t + W_{hg}h_{t-1} + b_g) \quad (14)$$

$$o_t = \sigma(W_{io}x_t + W_{ho}h_{t-1} + b_o) \quad (15)$$

$$c_t = f_t \odot c_{t-1} + i_t \odot g_t \quad (16)$$

$$h_t = o_t \odot \tanh(c_t) \quad (17)$$

Where \odot is the Hadamard product, σ and \tanh are the sigmoid and hyperbolic tangent activation functions. A hidden state at time t is represented by $h_t \in \mathbb{R}^Q$, a cell state is represented by $c_t \in \mathbb{R}^Q$, an input is represented by $x_t \in \mathbb{R}^M$ where M is the input vector dimension, and a hidden state at time $t-1$ is represented by h_{t-1} . Input, forget, cell, and output gates are represented by $i_t \in \mathbb{R}^Q$, $f_t \in \mathbb{R}^Q$, $g_t \in \mathbb{R}^Q$, and o_t respectively; $W_{ii} \in \mathbb{R}^{Q \times M}$, $W_{if} \in \mathbb{R}^{Q \times M}$, $W_{ig} \in \mathbb{R}^{Q \times M}$, $W_{io} \in \mathbb{R}^{Q \times M}$, $W_{hi} \in \mathbb{R}^{Q \times Q}$, $W_{hf} \in \mathbb{R}^{Q \times Q}$, $W_{hg} \in \mathbb{R}^{Q \times Q}$, and $W_{ho} \in \mathbb{R}^{Q \times Q}$ are matrices of weights; and $b_i \in \mathbb{R}^Q$, $b_f \in \mathbb{R}^Q$, $b_g \in \mathbb{R}^Q$, and $b_o \in \mathbb{R}^Q$ are biases.

A popular alternative to LSTM is gated recurrent units (GRUs) [54]. GRUs are capable of alleviating the vanishing gradient problem in a very similar manner to LSTMs but are simpler and require fewer parameters and operations.

$$r_t = \sigma(W_{ir}x_t + W_{hr}h_{t-1} + b_r) \quad (18)$$

$$z_t = \sigma(W_{iz}x_t + W_{hz}h_{t-1} + b_z) \quad (19)$$

$$n_t = \tanh(W_{in}x_t + b_{in} + r_t \odot (W_{hn}h_{t-1} + b_{hn})) \quad (20)$$

$$h_t = (1 - z_t) \odot n_t + z_t \odot h_{t-1} \quad (21)$$

Where $r_t \in \mathbb{R}^Q$, $z_t \in \mathbb{R}^Q$, $n_t \in \mathbb{R}^Q$ are the reset, update, and new gates, respectively; $W_{ir} \in \mathbb{R}^{Q \times M}$, $W_{iz} \in \mathbb{R}^{Q \times M}$, $W_{in} \in \mathbb{R}^{Q \times M}$, $W_{hr} \in \mathbb{R}^{Q \times Q}$, $W_{hz} \in \mathbb{R}^{Q \times Q}$, and $W_{hn} \in \mathbb{R}^{Q \times Q}$ are weights matrices; and $b_r \in \mathbb{R}^Q$, $b_z \in \mathbb{R}^Q$, $b_{in} \in \mathbb{R}^Q$, and $b_{hn} \in \mathbb{R}^Q$ are bias vectors.

4.1.2.2 RNNs with Extended Structures: We have implemented each architecture in a bidirectional manner with multiple RNN layers. In order to obtain a bidirectional structure, one RNN has to run in the forward direction, while the other one has to run in the reverse direction. An output of the bidirectional structure is the concatenation of the hidden states of both RNNs that correspond to the same time. In the single-layer case, the hidden state h_t of time t serves as an output of this unit, where in the multi-layer case, the input of $x_t^{(\ell)}$ of the ℓ^{th} layer is the hidden state $h_t^{(\ell-1)}$ of the previous layer.

4.1.3 Loss Function

We used the MS-TCN++ loss function, after adapting it to our prediction generator with ISR. This loss is defined as the sum of the prediction generation, which consists of the prediction heads losses, and the refinement stages losses. In total, the loss is $\mathcal{L} = \sum_{\eta} \mathcal{L}_{\eta}$, where η represents a prediction head, whether an ISR head or stages output head. The loss of each prediction head is defined as the weighted sum of the cross-entropy loss and a smoothing loss, formally defined as $\mathcal{L}_{\eta} = -\frac{1}{T} \sum_{t,c} y_{t,c} \log(\hat{y}_{t,c}) + \lambda \cdot \frac{1}{T \cdot C} \sum_{t,c} \Delta_{t,c}^2$, where λ determines the weight of the smoothing loss. The cross-entropy loss is $-\frac{1}{T} \sum_{t,c} y_{t,c} \log(\hat{y}_{t,c})$, where $\hat{y}_{t,c}$ represents the predicted probability for the class c at time point t , $y_{t,c} \in \{0, 1\}$ equals one if class c is the ground truth label otherwise, it is zero, and T is the total number of data points, i.e., the procedure length. The smoothing loss is $\frac{1}{T \cdot C} \sum_{t,c} \Delta_{t,c}^2$ where C is the total number of classes and $\Delta_{t,c}$ represents the bounded mean error over the procedure-wise log-probabilities. Formally, $\Delta_{t,c} = \min\{\tau, |\log \hat{y}_{t,c} - \log \hat{y}_{t-1,c}|\}$, where τ is a bounding parameter.

4.2 Data Augmentations

In this section, we present two data augmentations: *World frame Rotation* (WFR) to simulate data acquired when the world coordinate system is rotated, as a result, the position and orientation of each sensor in every data point are changed, and the *Horizontal Flip* (HF) augmentation where we simulate a work pattern of left-handed surgeons. For each procedure, during the training, each of the augmentations is applied independently in a probabilistic manner with probability p . These two data augmentations improve the generalization ability of our networks.

4.2.1 World frame Rotation Augmentation

Kinematic data is obtained by utilizing motion sensors that provide information on their pose in space for each timestamp, where pose refers to the sensor's location and orientation. Keep in mind that the poses of all sensors are interrelated as they are provided with respect to the same coordinate system. Thus, it is necessary to apply the same rotational operation across all sensors and timestamps in the sequence for creating the augmentation of a world frame of rotation. Our networks require orientation data in terms of intrinsic ZYX Euler angles. However, to apply the rotation to the sensor's pose, the orientation must be transformed into the form of the rotation matrix and eventually converted back to the Euler angles representation for input to the network. The Ascension trackSTAR system

includes multiple sensors whose coordinates are determined in relation to the coordinate system established with respect to the transmitter. In our two open surgery datasets, there are six sensors on the hands of the surgeon. Consider some sensor $s_i : i \in [6]$. In the JIGSAWS dataset, there are the left and right PSMs, where the PSM's data is identical to the sensor's data; hence, in this case, we will refer to PSM as a sensor. Such that for JIGSAWS $s_i : i \in [2]$. The sensor's pose at time t is determined by six degrees of freedom (6 DOF) $s_{i,t} = (x, y, z, e1, e2, e3)$, where $P_w^{s_{i,t}} = (x, y, z)$ is the position vector and $E_w^{s_{i,t}} = (e1, e2, e3) \in \mathbb{R}^3$ is the orientation vector represented by intrinsic ZYX Euler angles, with respect to world frame w that is established with respect to either the Ascension trackSTAR coordinate system or the da Vinci coordinate system. In addition to Euler angles, the orientation of each sensor can be represented by a rotation matrix $R_w^{s_{i,t}} \in \mathbb{R}^{3 \times 3}$, that represents the rotation from the world frame w to the $s_{i,t}$ sensor's frame. Let $\text{ROT}(E_w^{s_{i,t}}) = R_w^{s_{i,t}} : \mathbb{R}^3 \rightarrow \mathbb{R}^{3 \times 3}$ be a representation function from the Euler angles representation to the rotation matrices representation, and $\text{ROT}^{-1} : \mathbb{R}^{3 \times 3} \rightarrow \mathbb{R}^3$ be a function from the rotation matrices to Euler angle representation. Note, $\text{ROT}^{-1}(\cdot)$ function is not a mathematical inverse of $\text{ROT}(\cdot)$, since there is no one-to-one mapping between Euler angles and rotation matrices spaces; as such, these notations represent only the transformation between the two representations. Let w' be another world frame with the same origin as w ; namely, there is no translation between w and w' . The matrix that represents the rotation from the new world frame w' to the sensor's frame $s_{i,t}$ is given by $R_{w'}^{s_{i,t}} = R_{w'}^w R_w^{s_{i,t}} \in \mathbb{R}^3$, where $R_{w'}^w$ is our *augmentation matrix*. The new position vector with respect to the new world frame w' is obtained by $P_{w'}^{s_{i,t}} = R_{w'}^w \cdot P_w^{s_{i,t}} \in \mathbb{R}^3$. Let θ_{max} be the maximum allowed rotation angle. First of all, we select uniformly at random three Euler angles $E_{w'}^w = (e'_1, e'_2, e'_3)$ such that $e'_i \in [-\theta_{max}, \theta_{max}]$. Then, based on these three Euler angles we calculate the augmentation matrix $R_{w'}^w = \text{ROT}(E_{w'}^w)$. To change the orientation of the entire procedure, it is required to apply the same augmentation matrix on all six sensors for each time point, such that for each sensor, for each data point we calculate $R_w^{s_{i,t}} = \text{ROT}(E_w^{s_{i,t}})$. Then we obtain the sensor orientation with respect to the new world frame by $R_{w'}^{s_{i,t}} = R_{w'}^w R_w^{s_{i,t}}$ and we get back the Euler angle representation by $E_{w'}^{s_{i,t}} = \text{ROT}^{-1}(R_{w'}^{s_{i,t}})$. The position vector with respect to the new world frame is obtained by $P_{w'}^{s_{i,t}} = R_{w'}^w \cdot P_w^{s_{i,t}}$.

4.2.2 Horizontal Flip Augmentation

The idea behind the *Horizontal Flip* (HF) augmentation is to switch between the left and right hand. This way, the behavior of right-handed surgeons looks like left-handed, and vice versa. In the video domain, when the video capturing is perpendicular to the surgeon, this augmentation is trivial. It requires only a horizontal flip of the image and a switch between the labels of the left and right hands (or objects). However, sensor data consist of poses that have 3D location and orientation that should be correctly reflected along a plane. Yet there is no trivial definition of this reflection plane.

To develop this augmentation, we will assume that the original axis of the data z is upward. Thus we will define

the reflection axis in the xy plane. We will then flip the xy positions across this axis while preserving the values in the z direction. In addition, we will rotate the orientation of all the sensors.

More specifically, in our open surgery datasets, three sensors were placed on each hand. Hence, we will first calculate for each hand the average location of the three sensors, for each timestamp t . Formally, let $\bar{P}_{L,t} = (P_w^{s1,t} + P_w^{s2,t} + P_w^{s3,t})/3$ and $\bar{P}_{R,t} = (P_w^{s4,t} + P_w^{s5,t} + P_w^{s6,t})/3$, where the left hand is denoted by L and the right hand by R . For the JIGSAWS dataset, we will use the left and right PSM's data as is, namely $\bar{P}_{L,t} = P_w^{s1,t}$ and $\bar{P}_{R,t} = P_w^{s2,t}$. For computational reasons, we first downsample our data points by a factor of 50.

Next, for each point, we consider only its projection on the xy plain. As such let $\bar{P}_{L,t}^{xy}$ be the projection on the xy plane of $\bar{P}_{L,t}$, and $\bar{P}_{R,t}^{xy}$ be the projection of $\bar{P}_{R,t}$. Next, we define the reflection axis, which will yield the reflection plane. This axis is the one that separates, in an optimal way, between the left and right-hand data points: $\bar{P}_{L,t}^{xy}$ and $\bar{P}_{R,t}^{xy}$. Inspired by [55], we will use a geometric interpretation of a linear SVM to calculate this separation. We then calculate the reflection axis χ that satisfies the linear equation $\chi : y = mx + b$. Next, we reflect the original sensors' data across the plane induced by this line, where we assume that z values are preserved. The Ref_{2D} reflection matrix, described by Eq.22, is derived from the angle ϕ of the line χ with the x -axis, such that $\phi = \arctan(m)$.

$$Ref_{2D}(\phi) = \begin{bmatrix} \cos 2\phi & \sin 2\phi \\ \sin 2\phi & -\cos 2\phi \end{bmatrix} \quad (22)$$

Since the z values are preserved, our 3D reflection matrix is given by Eq.23.

$$Ref_{3D}(\phi) = \begin{bmatrix} \cos 2\phi & \sin 2\phi & 0 \\ \sin 2\phi & -\cos 2\phi & 0 \\ 0 & 0 & 1 \end{bmatrix} \quad (23)$$

Since our reflection line χ has a bias element b , for every sensor position $P_w^{s_i,t} = (x, y, z)$ we will subtract the bias, resulting $P_w^{s_i,t} = (x, y - b, z)$. Where \bar{w} is the world frame after this translation. The next step is to apply the reflection matrix on each position vector. Let us denote the reflected world frame by $w_{Ref'}$, then $P_{w_{Ref'}}^{s_i,t} = Ref_{3D}(\phi) \cdot P_w^{s_i,t} = (x_{Ref'}, y_{Ref'}, z_{Ref'}) \in \mathbb{R}^3$; notice that $Ref_{3D}(\phi) \in \mathbb{R}^{3 \times 3}$ is a matrix, and $P_w^{s_i,t} \in \mathbb{R}^3$ is a vector. To calculate the final portion vector we will add back the bias: $P_{w_{Ref}}^{s_i,t} = (x_{Ref'}, y_{Ref'} + b, z_{Ref'})$, where w_{Ref} is the final reflected world frame.

Position augmentation will be followed by augmentation of the sensor orientation. For each sensor and timestamp, we will represent the orientation by its rotation matrix, namely for each $E_w^{s_i,t}$ we will obtain $R_w^{s_i,t} = \text{ROT}(E_w^{s_i,t}) \in \mathbb{R}^{3 \times 3}$. Then, we will obtain the reflected orientation in rotation matrix representation by multiplying this matrix by our reflection matrix, such that $R_{w_{Ref}}^{s_i,t} = R_w^{s_i,t} \cdot Ref_{3D}(\phi)$. Then, we calculate the reflected Euler angles representation by $E_{w_{Ref}}^{s_i,t} = \text{ROT}^{-1}(R_{w_{Ref}}^{s_i,t})$. Finally, we exchanged between the right hand and the left hand of the surgeon, such that for our open surgery datasets sensor 1 was switched with sensor 4, sensor 2 was switched with sensor 5, and sensor 3

was exchanged with sensor 6. For JIGSAWS datasets the left PSM was switched with the right PSM.

5 EXPERIMENTS

5.1 Data Flow

Based on previous studies, velocities are the most beneficial input to an algorithm for analyzing kinematic data. Our augmentations must, however, be applied at absolute locations and orientations. Hence, as raw data we used locations and Euler angles, then applied our augmentations, and finally, before feeding the input into the algorithm, we calculated the velocities and normalized the data. Kinematic data in the JIGSAWS dataset do not include Euler angles, but rather rotation matrices. Based on these rotation matrices, we calculated the intrinsic Euler angles as a preprocessing step.

5.1.1 Velocities Calculation

For all three datasets, based on the Euler angles and positions, for each coordinate, the differences between every two adjacent timestamps were calculated; thus the input was the calculated linear and angular velocities.

5.1.2 Normalization

For each coordinate j in the input sequence, the data were normalized using the Standard score, formally defined as

$$\hat{\xi}_{1:T}^j = \frac{\xi_{1:T}^j - \bar{\xi}^j}{S^j} \quad (24)$$

where $\xi_{1:T}^j \in \mathbb{R}^T$ is a vector representing the non-normalized input data values, $\hat{\xi}_{1:T}^j \in \mathbb{R}^T$ the normalized data values, $\bar{\xi}^j$ the mean, and S the standard deviations of the elements of $\xi_{1:T}^j \in \mathbb{R}^T$, where $\bar{\xi}^j$ and S are calculated separately for each procedure.

5.2 Evaluation Metrics

A variety of metrics were used for model evaluation. These metrics can be divided into two groups: frame-wise metrics and segmentation metrics. Frame-wise metrics include Accuracy and Macro F1, which are more suitable in cases when the classes are imbalanced. The second group of metrics is the segmentation metrics which include edit distance¹ that is normalized by dividing the maximum between the ground truth's and the prediction's length at the instance level [4], and F1@k with $k \in \{10, 25, 50\}$ [3]. In the evaluation process, the intersection over union (IoU) between each predicted segment and the available ground truth segments was calculated. Whenever we found a ground truth segment with an IoU greater than k with the predicted segment, we marked this predicted segment as true positive and marked this ground truth segment as unavailable for use in the future. A false positive is defined as a prediction that does not match any available ground truth segment. The F1 score was calculated based on these calculations. Each metric was calculated for each performed procedure and the average was taken across all of the procedures.

1. In [56] marked as Edit*.

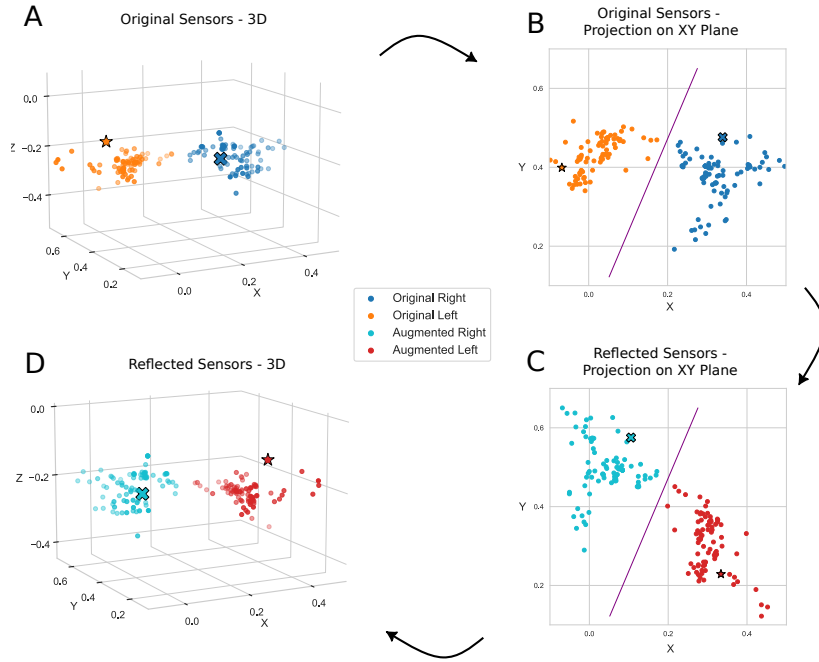


Fig. 6. Sample points from two sensors, one on each hand, illustrating the Horizontal Flip augmentation. The star- and cross-shaped points emphasize the transformations. The reflection plane given by the SVM output is represented by the purple line. **A** shows the original points in 3D, and **B** in the XY plane projection. The flipped points are shown in the XY plane in **C** and in 3D in **D**. Augmentation of orientation is not displayed.

5.3 Evaluation Method

All models trained on the VTS and BRS datasets were evaluated using 5-fold cross-validation. We divided the sequences on the participants' level, ensuring that if a participant had more than one procedure, they all belonged to the same fold. Consider the i^{th} fold. The sequences that belong to this fold constitute the test set of the fold. Two groups of participants were formed from the remaining sequences: one for the training set and one for the validation set. We used the validation set, which contains procedures from the $(i + 1)/mod5$ fold, to tune hyperparameters and determine where to stop the training process. This way, just as test sets are disjointed at the participants' level, so are validation sets. In the VTS dataset, three participants (12 procedures) have been selected from the $(i + 1)/mod5$ fold, for the validation set, and in the BRS dataset, five participants have been chosen. In the case of JIGSAWS, a standardized leave-one-user-out cross-validation is used to evaluate automatic surgical gesture recognition as defined in [15]. In addition, in VTS dataset evaluation, for a fair comparison to the results reported in [8], we used the same dataset and setting as in [8]. Namely, there are 96 procedures in the dataset. The left-handed surgeon was used to evaluate the HF augmentation separately from the entire dataset.

5.4 Test Set Performance

To ensure the stability of the networks, in addition to cross-validation, multiple random seeds were used [57]. Eight different seeds were used for the VTS dataset and six for the BRS dataset. The reported results for each metric are the mean and the standard deviation across all procedures of the dataset and all random seeds. In the case of VTS dataset,

there are $96 \text{ procedures} \times 8 \text{ seeds}$, and in the case of BRS dataset, there are $52 \text{ procedures} \times 6 \text{ seeds}$.

In both datasets, networks were trained for 40 epochs unless Horizontal Flip augmentation was applied, in which case 80 epochs were trained. In the case of JIGSAWS, only the predetermined seed was used, as it had been acceptable in previous studies. To ensure the convergence of our algorithms on the JIGSAWS dataset we trained the networks for 60 epochs; where Horizontal Flip augmentation was applied, we trained for 90 epochs. Note that the reported results are the results obtained in the last epoch. In addition, only in the JIGSAWS dataset training, we used a scheduler that reduced the learning rate by a factor of 2 when a loss stopped improving for 3 consecutive epochs.

5.5 Hyperparameter Tuning

The hyperparameter optimization was executed only on the VTS dataset on both our MS-TCN-BiLSTM and MS-TCN-BiGRU networks using the Optuna environment [58] with the TPESampler sampler for 300 trials. The following hyperparameters were tuned and associated with the prediction generator (PG): TCN dropout probability in the range of $[0.5, 0.7]$, number of layers in the PG out of $\{7, 9, 11, 13\}$, number of feature maps in the PG out of $\{32, 64, 128, 256\}$. The following hyperparameters were tuned and associated with the refinement module: number of refinement stages out of $\{1, 2, 3\}$, RNN dropout probability in the range of $[0.5, 0.7]$, RNN hidden dimension size out of $\{128, 256, 512\}$, number of RNN layers out of $\{1, 2\}$. The following hyperparameters were tuned and associated with the entire network: learning rate in the range of $[10^{-4}, 5 \cdot 10^{-3}]$, loss hyper parameter λ in the range of $[0.15, 1]$, batch size in the range of $[1, 5]$, primary sampling

factor r in the range of $[1, 8]$, and secondary sampling factor in the range of $[1, \lfloor 8/r \rfloor]$, where the sampling rates are factors that define how many samples are required to skip. The primary sampling factor is the downsample that is applied to the input of the network, and the secondary sampling factor refers to the downsampling performed in the refinement stages on the previous stage output. The number of epochs was 40; Adam optimizers were used to train all networks with $\beta_1 = 0.9$ and $\beta_2 = 0.999$. Eight Nvidia A100 GPUs were used for training and evaluation on a DGX Cluster. The optimal hyperparameters for each of our networks are described in Table 1. The optimized MS-TCN-BiLSTM network achieved a mean F1-Macro of 80.9 on the validation set with 6.3×10^6 parameters and the obtained MS-TCN-BiGRU attained a mean F1-Macro of 81.2 with 8.4×10^6 parameters. On all datasets, we used the optimized networks as described in this section without any additional hyperparameter tuning.

TABLE 1

Selected hyperparameters based on the VTS validation set, used for all other evaluations as-is.

	MS-TCN-LSTM	MS-TCN-GRU
Number of layers (PG)	11	13
Number of feature maps (PG)	256	256
Dropout (PG)	0.546	0.645
Number of refinement stages (Refinement)	1	1
Number of layers (Refinement)	2	2
Dropout (Refinement)	0.619	0.5747
Hidden dimension size (Refinement)	128	256
Learning rate	0.001035	0.001779
Primary sampling rate	2	1
Secondary sampling rate	3	6
λ	0.933	0.638
Number of parameters	6.3×10^6	8.4×10^6

5.6 Ablation Study

In this section, we investigate the performance of our networks by replacing certain components in order to understand the contribution of each component to the overall system. We started with MS-TCN++ adapted to kinematic data as proposed in [8], then we replaced every element in the architecture and measured the impact of this change. Note that we are able to use this method since we preserved the multi-stage framework of the architecture and replaced one component with another one that plays the same role. First of all, we replaced the standard prediction generator with our prediction generator which includes the ISR. It was found, as expected, that this step contributes to frame-wise metrics, but unfortunately at the expense of segmental metrics. Next, we showed that replacing the refinement stages with our RNN-based refinements improves the segmental performance of the networks; this result is also in line with our assumptions during the development of these refinement stages. Finally, we showed that procedure-wise normalization contributes to the performance of our proposed networks. Note that in [8], the mean and the standard deviation were calculated a priori based on the whole train set for each fold individually, instead of for each sequence separately. Table 2 summarizes the impact of each

modification on the architecture. We found that each of the modifications contributes to the overall system in at least one type of metric.

TABLE 2

Ablation study of the proposed architectures on the gesture recognition task of the VTS dataset - without data augmentation. * represents experiments using the normalization method from [8].

VTS	F1-macro	Acc	Edit	F1@10	F1@25	F1@50
MS-TCN++* [8]	78.9	82.4	86.3	89.3	85.8	71.1
MS TCN++ ISR*	79.8	83.3	81.7	86.2	82.8	68.6
MS-TCN-BiLSTM*	79.5	83	88.2	91	87.7	73.2
MS-TCN-BiGRU*	79.9	83.1	89.3	91.5	87.8	73.4
MS-TCN-BiLSTM	80.4	83.7	87.7	91.1	88.2	75.1
MS-TCN-BiGRU	80.9	84.1	89.0	91.7	88.7	75.5

5.7 BRS Dataset Baseline Establishing

Since the BRS dataset is introduced here for the first time for action segmentation without previously reported results, we established a baseline by training an MS-TCN++ model with the procedure-wise normalization method. We then compared this baseline to the MS-TCN-BiGRU and MS-TCN-BiLSTM models that we propose. The results are presented in Table 3. We found that the standard MS-TCN++ has significant difficulty with segmental metrics on this dataset, but both our architectures performed significantly better. The performance gap between MS-TCN++ and our algorithms in the BRS dataset is larger, highlighting the generalization advantages of our approach.

TABLE 3

Comparison between MS-TCN++, MS-TCN-BiGRU, and MS-TCN-BiLSTM on the BRS dataset.

BRS	F1-macro	Acc	Edit	F1@10	F1@25	F1@50
MS-TCN++	64.4	76.7	45.8	52.7	49.4	37.9
MS-TCN-BiGRU	64.8	77.4	75.8	77.4	72.9	57.6
MS-TCN-BiLSTM	65.9	77.8	75.1	77.3	73.1	57.1

5.8 World Frame Rotation

In this section, we present the effect of our WFR augmentation. We performed several experiments on each of the datasets. In the first experiment, we predefined that $\theta_{max} = 7^\circ$ and evaluated the effect of the probability of activating the augmentation. This experiment was performed on the VTS and BRS datasets. The results of this experiment are presented in Table 4. In general, we observe that the effect of this augmentation is noticeable on the BRS dataset but almost negligible on the VTS dataset. The difference in the effect of this augmentation on both datasets can probably be explained by the different methods by which the data were collected. While in VTS, data collection was performed only at one simulation station; in BRS there were eight stations. This might have resulted in some variance between the positioning of the transmitters at different stations. Note that these transmitters define the coordinate frame. Therefore, the ability to generalize the world frame angle contributes to the algorithm’s performance on this type of data. For both models on the BRS dataset, the algorithm performed best

when the augmentation was activated for each sequence with a probability of one. Note that during the evaluation, we do not apply augmentations.

TABLE 4

WFR augmentation evaluation on the VTS and BRS datasets. θ_{max} is fixed at 7° and the augmentation is applied at different probabilities.

VTS	prob	F1-macro	Acc	Edit	F1@10	F1@25	F1@50
MS-TCN-BiGRU	0	80.9	84.1	89.0	91.7	88.7	75.5
	0.5	80.7	83.9	89.0	91.8	88.7	75.4
	1	80.2	83.5	88.4	91.4	88.6	75.1
MS-TCN-BiLSTM	0	80.4	83.7	87.7	91.1	88.2	75.1
	0.5	80.8	84.2	88.6	91.7	89.2	76.1
	1	80.0	83.4	88.4	91.5	88.7	75.2
BRS	prob	F1-macro	Acc	Edit	F1@10	F1@25	F1@50
MS-TCN-BiGRU	0	64.8	77.4	75.8	77.4	72.9	57.6
	0.5	67.4	78.8	77.0	79.2	75.1	59.4
	1	68.0	78.7	77.7	79.4	75.0	59.3
MS-TCN-BiLSTM	0	65.9	77.8	75.1	77.3	73.1	57.1
	0.5	67.1	78.5	76.8	78.5	74.3	58.4
	1	68.5	79.2	77.3	79.2	75.2	59.3

Next, we evaluate the effect of θ_{max} on the performance of our networks, on the BRS dataset. We predetermined that the world frame rotation will be applied with a probability of one. We examine $\theta_{max} \in \{0^\circ, 7^\circ, 15^\circ\}$. The results are reported in Table 5. We found that both algorithms performed best with $\theta_{max} = 7^\circ$. In addition, note that besides the effect on the mean performance values, the standard deviations are also reduced by this augmentation. This is suggestive of the improvement in the algorithm’s robustness.

TABLE 5

WFR augmentation evaluation on the BRS dataset, with varying degrees of θ_{max} . The augmentation was applied with a probability of one.

θ_{max}	F1-macro	Acc	Edit	F1@10	F1@25	F1@50
MS-TCN-BiGRU						
0°	64.8 ± 13.5	77.3 ± 8.7	75.8 ± 9.9	77.4 ± 10.1	72.9 ± 11.7	57.6 ± 14.6
7°	68.0 ± 12.9	78.7 ± 8.0	77.7 ± 10.0	79.4 ± 9.9	75.0 ± 12.2	59.3 ± 14.6
15°	67.8 ± 12.0	79.0 ± 7.5	77.7 ± 10.1	79.1 ± 9.6	75.3 ± 11.2	60.0 ± 14.6
MS-TCN-BiLSTM						
0°	65.9 ± 14.1	77.8 ± 8.9	75.1 ± 10.7	77.3 ± 11.1	73.1 ± 12.5	57.1 ± 15.1
7°	68.5 ± 13.1	79.2 ± 8.5	77.3 ± 10.0	79.2 ± 10.6	75.2 ± 12.4	59.3 ± 14.7
15°	67.8 ± 13.3	78.9 ± 8.5	76.9 ± 10.1	79.1 ± 10.2	75.3 ± 12.0	59.9 ± 14.9

5.9 Horizontal Flip Effect

Here we analyze the effect of the HF augmentation on the VTS and BRS datasets. We do not evaluate this augmentation on the JIGSAWS dataset since there are no left-handed surgeons included in this dataset. In addition, in Goldbraikh et al. [8], the single left-handed surgeon in VTS data was excluded from the dataset. To enable direct comparison of the algorithms’ performance to the results reported in [8], we evaluate the effect of our augmentation on this data separately from the main results. This augmentation is applied with a probability of 0.5, thereby generating a pseudo-balanced dataset between left and right-handed surgeons. Due to the low representation of left-handed surgeons in clinics, and as a result a low representation in most datasets, this augmentation is of

paramount importance since it helps overcome the problem of low performance of deep learning systems in this group.

First, we examine the effect of the HF augmentation on the left-handed surgeon who was excluded from the VTS dataset in [8]. Namely, the left-handed surgeon’s four procedures served as a test set for all folds, where the train and validation sets stay standard as defined in Sec. 5.3. The results are presented in Table 6. Clearly, both networks had difficulties generalizing on left-handed surgeons without this augmentation. Through the use of this augmentation, we were able to achieve comparable performance to our regular test set, namely right-handed surgeons.

TABLE 6

HF evaluation on the left-handed surgeon from the VTS dataset. This surgeon was excluded from the VTS dataset in [8] and in all VTS parts in this work except the current experiment. In this experiment, this surgeon’s procedures were not part of the train or validation sets and are used as a test set, for each of the five regular folds.

VTS	HF	F1-macro	Acc	Edit	F1@10	F1@25	F1@50
MS-TCN-BiGRU		26.7	45.9	34.2	32.8	25.2	12.7
	✓	79.9	84.3	85.0	90.1	88.1	77.8
MS-TCN-BiLSTM		32.1	48.5	43.0	39.1	31.1	14.3
	✓	77.6	83.0	81.6	87.2	85.3	72.5

Next, we examine the Horizontal Flip effect on our networks and the effect of combining the Horizontal Flip and world frame rotation augmentation, with $\theta_{max} = 7^\circ$ and probability of activation 1. Notice, the results of this experiment are based on the standard test sets, while three left-handed surgeons are included in this dataset. Thus, the results of this experiment are valid when compared with the results reported in previous sections regarding the BRS dataset. We found that Horizontal Flip affects the convergence time of the training process, hence we trained here for 80 epochs. The results are presented in Table 7. For both networks, usage of this augmentation leads to an increase in the mean performance and a decrease in standard deviation. MS-TCN-BiLSTM exhibited additional improvement in network performance when we combined the HF with WFR augmentations during the training, yielding the best network on this dataset.

Finally, we analyzed the effect of our HF augmentation when it was conditioned on the handedness of the surgeon. The results are shown in Fig.7 on the MS-TCN-BiLSTM network, and on the MS-TCN-BiGRU can be found in Fig.8. In general, the results are similar to the results obtained on the VTS dataset in Table 6, where the augmentation dramatically affects the left-handed surgeons, such that the algorithm performed on both left- and right-handed surgeons with similar success. On the other hand, there was only a slight effect on the right-handed surgeon. Therefore, we can conclude that augmentation makes the algorithm more robust by making it suitable for both left-handed and right-handed surgeons. This can explain the fact that standard deviations decreased as well.

5.10 JIGSAWS Evaluation

The purpose of this experiment is to evaluate the impact of the augmentations on the performance of our algorithms on

TABLE 7

The effect of HF and HF+ WFR together. The HF augmentation was applied with a probability of 0.5; for WFR, θ_{max} is fixed at 7° and the augmentation was applied with a probability of one.

BRS	F1-macro	Acc	Edit	F1@10	F1@25	F1@50
MS-TCN-BiGRU						
Baseline	64.8 ± 13.5	77.4 ± 8.7	75.8 ± 9.9	77.4 ± 10.1	72.9 ± 11.7	57.6 ± 14.7
HF	68.4 ± 10.6	79.2 ± 6.6	78.9 ± 8.5	80.7 ± 8.5	76.8 ± 9.6	61.7 ± 13.0
HF + WFR	67.7 ± 11.0	78.9 ± 6.6	78.7 ± 8.1	80.6 ± 8.3	76.8 ± 9.8	61.5 ± 13.2
MS-TCN-BiLSTM						
Baseline	65.9 ± 14.1	77.8 ± 8.9	75.1 ± 10.7	77.3 ± 11.1	73.1 ± 12.5	57.1 ± 15.1
HF	69.4 ± 11.0	80.0 ± 6.4	78.7 ± 9.0	80.7 ± 8.6	77.1 ± 9.3	61.8 ± 12.8
HF + WFR	70.0 ± 10.8	80.5 ± 5.9	78.4 ± 9.5	81.1 ± 8.6	77.5 ± 9.3	62.5 ± 12.2

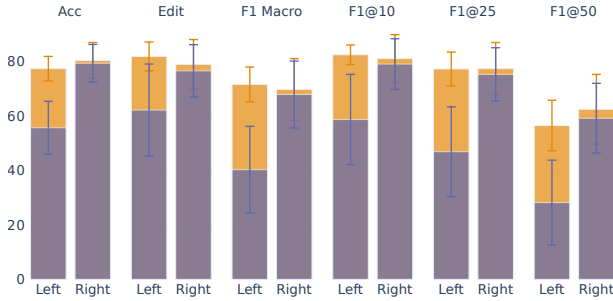


Fig. 7. Surgeons' performance conditioned by their handedness. Purple - without HF, Orange - the contribution of the HF augmentation. Evaluated on the MS-TCN-BiLSTM model and the BRS dataset. Error bars represent standard deviation.

the benchmark JIGSAWS dataset. For each of our architectures, we present the performance without augmentation, with WFR, and with both WFR and HF. In this experiment, we used WFR with $\theta_{max} = 7$, applied with a probability of one, and HF with applied with a probability of 0.5. The results are summarized in Table 8. In general, MS-TCN-BiGRU performs better than MS-TCN-BiLSTM. Adding augmentations to both networks improves their baseline performance, except for the addition of HF to MS-TCN-BiLSTM which has no effect on overall performance. On the other hand, using both augmentations with MS-TCN-BiGRU at the same time is much more effective and yields the best results compared to all other alternatives. Due to the lack of left-handed surgeons in the JIGSAWS dataset, the high effectiveness of HF augmentation is surprising. In this dataset, we speculate that the effect of this augmentation is due to improved generalization capabilities during training.

TABLE 8

The effect of augmentations in evaluation on the JIGSAWS dataset.

Where WFR was used, θ_{max} was fixed at 7° , and applying the augmentation was with a probability of one. When HF was used, it was applied with a probability of 0.5

JIGSAWS	F1-macro	Acc	Edit	F1@10	F1@25	F1@50
MS-TCN-BiLSTM						
Baseline	77.7 ± 13.7	84.2 ± 10.7	88.2 ± 13.8	91.6 ± 10.3	90.8 ± 11.4	85.3 ± 15.0
WFR	78.5 ± 13.0	84.8 ± 10.0	86.9 ± 13.5	91.0 ± 10.1	90.4 ± 11.3	84.0 ± 15.3
WFR+HF	78.1 ± 12.5	84.6 ± 9.2	87.9 ± 12.8	91.7 ± 9.5	90.4 ± 11.0	83.7 ± 15.7
MS-TCN-BiGRU						
Baseline	79.2 ± 12.2	85.0 ± 10.1	87.7 ± 10.2	91.4 ± 8.7	90.6 ± 9.9	85.1 ± 14.0
WFR	80.0 ± 11.9	85.5 ± 9.0	90.1 ± 10.4	93.3 ± 8.0	92.6 ± 8.8	86.4 ± 13.5
WFR+HF	81.8 ± 11.2	86.4 ± 7.3	90.5 ± 11.4	94.1 ± 7.5	93.6 ± 8.1	87.0 ± 13.1

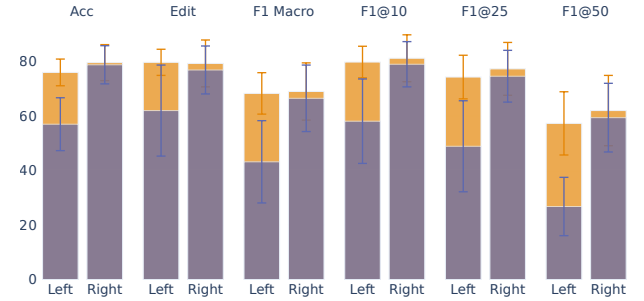


Fig. 8. MS-TCN-BiGRU model, surgeons' performance is conditioned by their handedness. Purple - without HF, Orange - the contribution of the HF augmentation. Evaluated on BRS dataset. The standard deviation is represented by error bars.

5.11 Comparison with The State-Of-The-Art

In this section, we compare our best algorithms with previous state-of-the-art (SOTA) algorithms reported in the literature on the VTS and JIGSAWS datasets. The results are shown in Table 9. First of all, we can conclude that for the VTS dataset both our algorithms outperform the reference algorithms from [8], including the Multi-task (MT) versions which used additional labeling during the training process, whereas the MS-TCN-BiGRU established the new benchmark result on this data set. On the JIGSAWS dataset, for the kinematic modality, MS-TCN-BiGRU with the WFR-HF augmentation established new SOTA results on all metrics. Notice that part of the compared networks used the original JIGSAWS labels, which contain labeling errors, which have been corrected since 2020 in [11]. Using our MS-TCN-BiGRU with WFR+HF, the accuracy of MS-TCN-BiGRU is improved by 0.9, and the edit is improved by 2. Note that previous SOTA results were achieved by two different networks, one for each metric. Here, a significant advance is demonstrated over the SOTA which was previously demonstrated, achieved by a single network.

TABLE 9

Comparison to state-of-the-art results on the VTS and JIGSAWS datasets, for models trained on kinematic data only. Models marked with an * are based on the original JIGSAWS labels.

VTS	F1-macro	Acc	Edit	F1@10	F1@25	F1@50
BiGRU [8]	78.2 ± 8.8	82.2 ± 7.3	84.9 ± 7.7	88.0 ± 7.0	83.8 ± 10.2	68.9 ± 18.3
BiLSTM [8]	77.1 ± 9.3	81.3 ± 7.5	84.7 ± 8.2	88.1 ± 7.3	83.7 ± 10.4	68.1 ± 18.7
MS-TCN++ [8]	78.9 ± 8.5	82.4 ± 7.0	86.3 ± 8.4	89.3 ± 7.0	85.8 ± 9.8	71.1 ± 17.9
MT BiGRU [8]	78.2 ± 8.7	82.2 ± 7.0	85.4 ± 7.4	88.1 ± 6.8	83.9 ± 9.8	69.0 ± 18.1
MT BiLSTM [8]	75.7 ± 9.3	79.9 ± 7.6	83.3 ± 9.0	86.4 ± 8.3	81.9 ± 11.4	65.9 ± 18.8
MT MS-TCN++ [8]	78.5 ± 8.2	82.4 ± 6.6	86.0 ± 8.5	89.1 ± 7.5	85.8 ± 10.0	71.4 ± 17.5
MS-TCN-BiLSTM	80.4 ± 7.7	83.7 ± 6.3	87.7 ± 8.2	91.1 ± 6.7	88.2 ± 9.2	75.1 ± 16.8
MS-TCN-BiGRU	80.9 ± 8.0	84.1 ± 6.7	89.0 ± 7.7	91.7 ± 6.3	88.7 ± 9.4	75.5 ± 17.6
JIGSAWS						
	F1-macro	Acc	Edit	F1@10	F1@25	F1@50
BiLSTM* [9]	-	84.7	88.1	-	-	-
BiGRU* [9]	-	84.8	88.5	-	-	-
TCN + RL* [7]	-	82.1	87.9	91.1	89.5	82.3
APc [11]	-	85.5	85.3	-	-	-
MS-TCN-BiGRU+ +WFR+HF	81.8 ± 11.2	86.4 ± 7.3	90.5 ± 11.4	94.1 ± 7.5	93.6 ± 8.1	87.0 ± 13.1

In Table 10 we go beyond kinematics-only based models, and compare our algorithm's performance to models based on video data or on multi-modal (kinematics+video) data. This comparison is done on models evaluated on the JIGSAWS dataset. In terms of Edit distance and F1@10 scores, our MS-TCN-BiGRU with the WFR+HF augmentation achieved second-place results, which are competitive

with the state-of-the-art results in a multimodal architecture that combines video with kinematic data that was published recently in 2022 [12]. In terms of accuracy, we achieved third place, with a 1.5-point gap to the state-of-the-art result. Furthermore, we have state-of-the-art results for F1@25 and F1@50, but not all recent publications report these metrics. In summary, our model outperforms all previous video-based algorithms and is competitive with multi-modal networks.

TABLE 10

Comparison of our algorithms, which were trained on kinematic data to state-of-the-art results on the JIGSAWS dataset, to models trained on video and multi-modal data. Models marked with * are based on the original JIGSAWS labels. Models marked with † were implemented by [6]. During the training of our models, we used WFR+HF augmentation.

The WFR augmentation was applied with a probability of one, with $\theta_{max} = 7^\circ$. HF was applied with a probability of 0.5. The best results are in bold, the second place is marked by underlining.

	Modality		Acc	Edit	F1@10	F1@25	F1@50
	Kin	Vid					
C3D-MTL-VF* [6]	✓		82.1	86.6	90.6	89.1	80.3
MS-TCN* [59] (implemented by [6])	✓		78.9	85.8	88.5	86.6	75.8
TCN + RL* [7]	✓		81.4	88	92	90.5	82.2
TDRN* [60]	✓		84.6	90.2	92.9	-	-
RL+Tree* [5]	✓		81.7	88.5	92.7	91.0	83.2
MRG-Net* [14]	✓	✓	87.9	89.3	-	-	-
Fusion-KV* [13]	✓	✓	86.3	87.2	-	-	-
MA-TCN [12]	✓	✓	<u>86.8</u>	91.4	94.3	-	-
MS-TCN-BiGRU+ +WFR+HF	✓		86.4	<u>90.5</u>	<u>94.1</u>	93.6	87.0

6 CONCLUSIONS

This work has a double target related to the action segmentation tasks on kinematic data. First, we presented two multi-stage architectures that by using kinematic data achieved state-of-the-art results on benchmark datasets. Second, we presented two new augmentations for kinematic data, based on the strong geometric structure of the data to improve the performance and robustness of obtained algorithms.

We evaluated our algorithms on three different datasets, including two open surgery simulations and one robotic surgery. We found that our algorithms performed well without dependency if the data were obtained from the da vinci robot or from electromagnetic sensors that had been located on the surgeon’s hands during the open surgery procedure. Despite the differences in the method of acquiring the data, the preprocessing process is almost similar to RAMIS and open surgery data.

Both architectures contain a TCN-based prediction generator with intra-stage regularization, which contributes to the frame-wise performance of the network. In our view, adding these prediction heads at a relatively low layer in the architecture allows the network to focus on a relatively small area around the prediction location, which is less affected by a long history. Then, we used RNN-based refinement stages, where downsampling was applied at the refinement stage’s entrance and upsampling at the refinement stage’s exit. These refinement units contributed to a reduction in over-segmentation errors. While downsampling reduces noise and fits frequencies to the range where RNNs operate optimally, upsampling restores the sequence to its original dimensions.

In addition, inspired by computer vision horizontal flip and 2D rotation augmentation, we developed two new augmentations for kinematic data, World-Frame Rotation and Horizontal Flip. First, a random rotation of the 3D coordinate frame contributes to generalization, which is reflected in an increase in mean performance and a decrease in standard deviation, especially in the complex BRS dataset. The second augmentation was the Horizontal Flip. This mathematically complex augmentation tries to overcome the under-representation problem of left-handed surgeons in most surgical action segmentation datasets. The network’s performance on left-handed surgeons improved dramatically as a result of this augmentation, without affecting the network’s performance on right-handed surgeons. Thus, the mean of the performance metrics increased and the standard deviation of the performances decreased, resulting in stronger and more robust algorithms.

Our MS-TCN-BiLSTM achieved the best results on the BRS dataset, which is the most diverse among our datasets for action recognition, containing 52 different surgeons, with different handedness. In this case, both our augmentations contributed to the algorithm’s performance. Our MS-TCN-BiGRU outperformed the current state-of-the-art on the JIGSAWS and VTS benchmark datasets. In the JIGSAWS case, it also outperformed algorithms that are based on video and is competitive with multi-modal data algorithms.

REFERENCES

- [1] S.-J. Li, Y. AbuFarha, Y. Liu, M.-M. Cheng, and J. Gall, “Ms-tcn++: Multi-stage temporal convolutional network for action segmentation,” *IEEE transactions on pattern analysis and machine intelligence*, 2020.
- [2] F. Yi, H. Wen, and T. Jiang, “Asformer: Transformer for action segmentation,” *arXiv preprint arXiv:2110.08568*, 2021.
- [3] C. Lea, M. D. Flynn, R. Vidal, A. Reiter, and G. D. Hager, “Temporal convolutional networks for action segmentation and detection,” in *proceedings of the IEEE Conference on Computer Vision and Pattern Recognition*, 2017, pp. 156–165.
- [4] C. Lea, R. Vidal, and G. D. Hager, “Learning convolutional action primitives for fine-grained action recognition,” in *2016 IEEE international conference on robotics and automation (ICRA)*. IEEE, 2016, pp. 1642–1649.
- [5] X. Gao, Y. Jin, Q. Dou, and P.-A. Heng, “Automatic gesture recognition in robot-assisted surgery with reinforcement learning and tree search,” in *2020 IEEE International Conference on Robotics and Automation (ICRA)*. IEEE, 2020, pp. 8440–8446.
- [6] T. Wang, Y. Wang, and M. Li, “Towards accurate and interpretable surgical skill assessment: A video-based method incorporating recognized surgical gestures and skill levels,” in *International Conference on Medical Image Computing and Computer-Assisted Intervention*. Springer, 2020, pp. 668–678.
- [7] D. Liu and T. Jiang, “Deep reinforcement learning for surgical gesture segmentation and classification,” in *International conference on medical image computing and computer-assisted intervention*. Springer, 2018, pp. 247–255.
- [8] A. Goldbraikh, T. Volk, C. M. Pugh, and S. Laufer, “Using open surgery simulation kinematic data for tool and gesture recognition,” *International Journal of Computer Assisted Radiology and Surgery*, pp. 1–15, 2022.
- [9] R. DiPietro, N. Ahmidi, A. Malpani, M. Waldram, G. I. Lee, M. R. Lee, S. S. Vedula, and G. D. Hager, “Segmenting and classifying activities in robot-assisted surgery with recurrent neural networks,” *International journal of computer assisted radiology and surgery*, vol. 14, no. 11, pp. 2005–2020, 2019.
- [10] R. DiPietro, C. Lea, A. Malpani, N. Ahmidi, S. S. Vedula, G. I. Lee, M. R. Lee, and G. D. Hager, “Recognizing surgical activities with recurrent neural networks,” in *International conference on medical image computing and computer-assisted intervention*. Springer, 2016, pp. 551–558.

- [11] B. van Amsterdam, M. J. Clarkson, and D. Stoyanov, "Multi-task recurrent neural network for surgical gesture recognition and progress prediction," in *2020 IEEE International Conference on Robotics and Automation (ICRA)*. IEEE, 2020, pp. 1380–1386.
- [12] B. Van Amsterdam, I. Funke, E. Edwards, S. Speidel, J. Collins, A. Sridhar, J. Kelly, M. J. Clarkson, and D. Stoyanov, "Gesture recognition in robotic surgery with multimodal attention," *IEEE Transactions on Medical Imaging*, 2022.
- [13] Y. Qin, S. A. Pedram, S. Feyzabadi, M. Allan, A. J. McLeod, J. W. Burdick, and M. Azizian, "Temporal segmentation of surgical sub-tasks through deep learning with multiple data sources," in *2020 IEEE International Conference on Robotics and Automation (ICRA)*. IEEE, 2020, pp. 371–377.
- [14] Y. Long, J. Y. Wu, B. Lu, Y. Jin, M. Unberath, Y.-H. Liu, P. A. Heng, and Q. Dou, "Relational graph learning on visual and kinematics embeddings for accurate gesture recognition in robotic surgery," in *2021 IEEE International Conference on Robotics and Automation (ICRA)*. IEEE, 2021, pp. 13 346–13 353.
- [15] Y. Gao, S. S. Vedula, C. E. Reiley, N. Ahmidi, B. Varadarajan, H. C. Lin, L. Tao, L. Zappella, B. Béjar, D. D. Yuh, C. C. G. Chen, R. Vida, S. Khudanpur, and G. G. Hager, "Jhu-isi gesture and skill assessment working set (jigsaws): A surgical activity dataset for human motion modeling," in *MICCAI workshop: M2cai*, vol. 3, 2014, p. 3.
- [16] R. Hachiuma, T. Shimizu, H. Saito, H. Kajita, and Y. Takatsume, "Deep selection: A fully supervised camera selection network for surgery recordings," in *International Conference on Medical Image Computing and Computer-Assisted Intervention*. Springer, 2020, pp. 419–428.
- [17] K. Basiev, A. Goldbraikh, C. M. Pugh, and S. Laufer, "Open surgery tool classification and hand utilization using a multi-camera system," *International Journal of Computer Assisted Radiology and Surgery*, vol. 17, no. 8, pp. 1497–1505, 2022.
- [18] M. Masuda, H. Saito, Y. Takatsume, and H. Kajita, "Novel view synthesis for surgical recording," in *MICCAI Workshop on Deep Generative Models*. Springer, 2022, pp. 67–76.
- [19] A. Goldbraikh, A.-L. D'Angelo, C. M. Pugh, and S. Laufer, "Video-based fully automatic assessment of open surgery suturing skills," *International Journal of Computer Assisted Radiology and Surgery*, pp. 1–12, 2022.
- [20] C. Perumalla, L. Kearse, M. Peven, S. Laufer, C. Goll, B. Wise, S. Yang, and C. Pugh, "Ai-based video segmentation: Procedural steps or basic maneuvers?" *Journal of Surgical Research*, vol. 283, pp. 500–506, 2023.
- [21] H. I. Fawaz, G. Forestier, J. Weber, L. Idoumghar, and P.-A. Muller, "Accurate and interpretable evaluation of surgical skills from kinematic data using fully convolutional neural networks," *International journal of computer assisted radiology and surgery*, vol. 14, no. 9, pp. 1611–1617, 2019.
- [22] C. Lea, R. Vidal, A. Reiter, and G. D. Hager, "Temporal convolutional networks: A unified approach to action segmentation," in *European Conference on Computer Vision*. Springer, 2016, pp. 47–54.
- [23] I. Funke, S. Bodenstedt, F. Oehme, F. von Bechtolsheim, J. Weitz, and S. Speidel, "Using 3d convolutional neural networks to learn spatiotemporal features for automatic surgical gesture recognition in video," in *International Conference on Medical Image Computing and Computer-Assisted Intervention*. Springer, 2019, pp. 467–475.
- [24] T. Chen, S. Kornblith, M. Norouzi, and G. Hinton, "A simple framework for contrastive learning of visual representations," in *International conference on machine learning*. PMLR, 2020, pp. 1597–1607.
- [25] J.-B. Grill, F. Strub, F. Altché, C. Tallec, P. Richemond, E. Buchatskaya, C. Doersch, B. Avila Pires, Z. Guo, M. Gheshlaghi Azar *et al.*, "Bootstrap your own latent—a new approach to self-supervised learning," *Advances in neural information processing systems*, vol. 33, pp. 21 271–21 284, 2020.
- [26] M. Caron, I. Misra, J. Mairal, P. Goyal, P. Bojanowski, and A. Joulin, "Unsupervised learning of visual features by contrasting cluster assignments," *Advances in Neural Information Processing Systems*, vol. 33, pp. 9912–9924, 2020.
- [27] M. Caron, H. Touvron, I. Misra, H. Jégou, J. Mairal, P. Bojanowski, and A. Joulin, "Emerging properties in self-supervised vision transformers," in *Proceedings of the IEEE/CVF International Conference on Computer Vision*, 2021, pp. 9650–9660.
- [28] A. Mikołajczyk and M. Grochowski, "Data augmentation for improving deep learning in image classification problem," in *2018 international interdisciplinary PhD workshop (IIPhDW)*. IEEE, 2018, pp. 117–122.
- [29] B. K. Iwana and S. Uchida, "An empirical survey of data augmentation for time series classification with neural networks," *Plos one*, vol. 16, no. 7, p. e0254841, 2021.
- [30] D. Itzkovich, Y. Sharon, A. Jarc, Y. Refaely, and I. Nisky, "Using augmentation to improve the robustness to rotation of deep learning segmentation in robotic-assisted surgical data," in *2019 International Conference on Robotics and Automation (ICRA)*. IEEE, 2019, pp. 5068–5075.
- [31] —, "Generalization of deep learning gesture classification in robotic-assisted surgical data: From dry lab to clinical-like data," *IEEE Journal of Biomedical and Health Informatics*, vol. 26, no. 3, pp. 1329–1340, 2021.
- [32] S. Karaman, L. Seidenari, and A. Del Bimbo, "Fast saliency based pooling of fisher encoded dense trajectories," in *ECCV THUMOS Workshop*, vol. 1, no. 2, 2014, p. 5.
- [33] M. Rohrbach, S. Amin, M. Andriluka, and B. Schiele, "A database for fine grained activity detection of cooking activities," in *2012 IEEE conference on computer vision and pattern recognition*. IEEE, 2012, pp. 1194–1201.
- [34] Y. Cheng, Q. Fan, S. Pankanti, and A. Choudhary, "Temporal sequence modeling for video event detection," in *Proceedings of the IEEE conference on computer vision and pattern recognition*, 2014, pp. 2227–2234.
- [35] H. Kuehne, A. Arslan, and T. Serre, "The language of actions: Recovering the syntax and semantics of goal-directed human activities," in *Proceedings of the IEEE conference on computer vision and pattern recognition*, 2014, pp. 780–787.
- [36] H. Kuehne, J. Gall, and T. Serre, "An end-to-end generative framework for video segmentation and recognition," in *2016 IEEE Winter Conference on Applications of Computer Vision (WACV)*. IEEE, 2016, pp. 1–8.
- [37] J. Yue-Hei Ng, M. Hausknecht, S. Vijayanarasimhan, O. Vinyals, R. Monga, and G. Toderici, "Beyond short snippets: Deep networks for video classification," in *Proceedings of the IEEE conference on computer vision and pattern recognition*, 2015, pp. 4694–4702.
- [38] J. Donahue, L. Anne Hendricks, S. Guadarrama, M. Rohrbach, S. Venugopalan, K. Saenko, and T. Darrell, "Long-term recurrent convolutional networks for visual recognition and description," in *Proceedings of the IEEE conference on computer vision and pattern recognition*, 2015, pp. 2625–2634.
- [39] J. Carreira and A. Zisserman, "Quo vadis, action recognition? a new model and the kinetics dataset," in *proceedings of the IEEE Conference on Computer Vision and Pattern Recognition*, 2017, pp. 6299–6308.
- [40] B. Varadarajan, C. Reiley, H. Lin, S. Khudanpur, and G. Hager, "Data-derived models for segmentation with application to surgical assessment and training," in *International Conference on Medical Image Computing and Computer-Assisted Intervention*. Springer, 2009, pp. 426–434.
- [41] L. Tao, L. Zappella, G. D. Hager, and R. Vidal, "Surgical gesture segmentation and recognition," in *International conference on medical image computing and computer-assisted intervention*. Springer, 2013, pp. 339–346.
- [42] E. Mavroudi, D. Bhaskara, S. Sefati, H. Ali, and R. Vidal, "End-to-end fine-grained action segmentation and recognition using conditional random field models and discriminative sparse coding," in *2018 IEEE Winter Conference on Applications of Computer Vision (WACV)*. IEEE, 2018, pp. 1558–1567.
- [43] G. Forestier, F. Petitjean, P. Senin, F. Despinoy, A. Hualmé, H. I. Fawaz, J. Weber, L. Idoumghar, P.-A. Muller, and P. Jannin, "Surgical motion analysis using discriminative interpretable patterns," *Artificial intelligence in medicine*, vol. 91, pp. 3–11, 2018.
- [44] S. Ashry, T. Ogawa, and W. Gomaa, "Charm-deep: Continuous human activity recognition model based on deep neural network using imu sensors of smartwatch," *IEEE Sensors Journal*, vol. 20, no. 15, pp. 8757–8770, 2020.
- [45] R. Huan, C. Jiang, L. Ge, J. Shu, Z. Zhan, P. Chen, K. Chi, and R. Liang, "Human complex activity recognition with sensor data using multiple features," *IEEE Sensors Journal*, vol. 22, no. 1, pp. 757–775, 2021.
- [46] Q. Wen, L. Sun, F. Yang, X. Song, J. Gao, X. Wang, and H. Xu, "Time series data augmentation for deep learning: A survey," *arXiv preprint arXiv:2002.12478*, 2020.
- [47] K. M. Rashid and J. Louis, "Times-series data augmentation and

- deep learning for construction equipment activity recognition," *Advanced Engineering Informatics*, vol. 42, p. 100944, 2019.
- [48] A. Goldbraikh, O. Shubi, N. Shamir, Carla, and S. Laufer, "Efficient assessment of surgical maneuvers: Human versus machine," in *2022 Surgeons and Engineers: A Dialogue on Surgical Simulation*. ACS, 2022.
- [49] A. Goldbraikh, A.-L. D. D'Angelo, C. M. Pugh, and S. Laufer, "Tool usage in open surgery video data," in *Computer Assisted Radiology and Surgery (CARS) 2020*, 2020.
- [50] A.-L. D. D'Angelo, D. N. Rutherford, R. D. Ray, S. Laufer, C. Kwan, E. R. Cohen, A. Mason, and C. M. Pugh, "Idle time: an underdeveloped performance metric for assessing surgical skill," *The American Journal of Surgery*, vol. 209, no. 4, pp. 645–651, 2015.
- [51] O. Friard and M. Gamba, "Boris: a free, versatile open-source event-logging software for video/audio coding and live observations," *Methods in ecology and evolution*, vol. 7, no. 11, pp. 1325–1330, 2016.
- [52] J. H. McClellan and T. W. Parks, "A personal history of the parksmcclellan algorithm," *IEEE signal processing magazine*, vol. 22, no. 2, pp. 82–86, 2005.
- [53] S. Hochreiter and J. Schmidhuber, "Long short-term memory," *Neural computation*, vol. 9, no. 8, pp. 1735–1780, 1997.
- [54] J. Chung, C. Gulcehre, K. Cho, and Y. Bengio, "Empirical evaluation of gated recurrent neural networks on sequence modeling," in *NIPS 2014 Workshop on Deep Learning, December 2014*, 2014.
- [55] N. Avisdris, B. Yehuda, O. Ben-Zvi, D. Link-Sourani, L. Ben-Sira, E. Miller, E. Zharkov, D. Ben Bashat, and L. Joskowicz, "Automatic linear measurements of the fetal brain on mri with deep neural networks," *International Journal of Computer Assisted Radiology and Surgery*, vol. 16, no. 9, pp. 1481–1492, 2021.
- [56] B. van Amsterdam, M. J. Clarkson, and D. Stoyanov, "Gesture recognition in robotic surgery: a review," *IEEE Transactions on Biomedical Engineering*, vol. 68, no. 6, 2021.
- [57] P. Madhyastha and R. Jain, "On model stability as a function of random seed," in *Proceedings of the 23rd Conference on Computational Natural Language Learning (CoNLL)*. Hong Kong, China: Association for Computational Linguistics, Nov. 2019, pp. 929–939. [Online]. Available: <https://aclanthology.org/K19-1087>
- [58] T. Akiba, S. Sano, T. Yanase, T. Ohta, and M. Koyama, "Optuna: A next-generation hyperparameter optimization framework," in *Proceedings of the 25th ACM SIGKDD International Conference on Knowledge Discovery and Data Mining*, 2019.
- [59] Y. A. Farha and J. Gall, "Ms-tcn: Multi-stage temporal convolutional network for action segmentation," in *Proceedings of the IEEE/CVF Conference on Computer Vision and Pattern Recognition*, 2019, pp. 3575–3584.
- [60] P. Lei and S. Todorovic, "Temporal deformable residual networks for action segmentation in videos," in *Proceedings of the IEEE conference on computer vision and pattern recognition*, 2018, pp. 6742–6751.